

Counter-rotating eddy pair in the Luzon Strait

Sun Ruili^{1,2*}, Li Peiliang^{1,3}, GuYanzhen³, Zhai Fangguo⁴, Yan Yunwei², Li Bo⁵

¹Hainan Institute of Zhejiang University, Sanya, Hainan, China

²State Key Laboratory of Satellite Ocean Environment Dynamics, Second Institute of Oceanography, Ministry of Natural Resources, Hangzhou, China

³Ocean college, Zhejiang University, Zhoushan, China

⁴College of Oceanic and Atmospheric Sciences, Ocean University of China, Qingdao, China

⁵State Key Laboratory of Tropical Oceanography, South China Sea Institute of Oceanology, Chinese Academy of Sciences, Guangzhou, China

Corresponding author: Sun Ruili, sunruili2007@126.com

Abstract:

Based on satellite remote-sensing observation data and Hybrid Coordinate Ocean Model (HYCOM) re-analysis data, we studied the counter-rotating eddy pair in the Luzon Strait (LS). Statistical analysis reveals that when an anti-cyclonic mesoscale eddy (AE) (cyclonic mesoscale eddy [CE]) in the Northwest Pacific (NWP) gradually approaches the east side of the LS, a CE (an AE) gradually forms on the west side of the LS, and it is defined as the AE (CE) mode of the counter-rotating eddy pair in the LS. The counter-rotating eddy pair exhibits obvious seasonal variation: the AE mode mainly occurs in the summer half of the year, while the CE mode mainly occurs in the winter half of the year. The mean durations of the AE and CE modes are both approximately 70 d. Based on vorticity budget equation and energy analysis, the dynamic mechanism of counter-rotating eddy-pair occurrence is determined to be as follows: the AE (CE)

23 on the east side of the LS causes a positive (negative) vorticity anomaly through horizontal
24 velocity shear on the west side of the LS, and the positive (negative) vorticity anomaly is
25 transported westward by the zonal advection of the vorticity, finally leading to the formation of the
26 CE (AE) on the west side of the LS.

27 **Keywords:** counter-rotating eddy pair; Luzon Strait; vorticity budget equation; barotropic
28 instability

29 **1 Introduction**

30 The Luzon Strait (LS), located between the island of Taiwan and Luzon Island, is an important
31 gap for particle and energy exchange between the South China Sea (SCS) and Northwest Pacific
32 (NWP). The topography around the LS is very complicated. The LS is composed of three straits
33 from north to south: Bashi Strait, Balintang Strait, and Babuyan Strait. The Batanes Islands and
34 Babuyan Islands are located in these straits (Figure 1). This complex topography leads to the
35 generation and aggregation of a large number of mesoscale eddies, which then play an important
36 role in the dynamic ocean process around the LS (Liu *et al.*, 2012; Lu and Liu, 2013; Sun *et al.*,
37 2016a; Sun *et al.*, 2020).

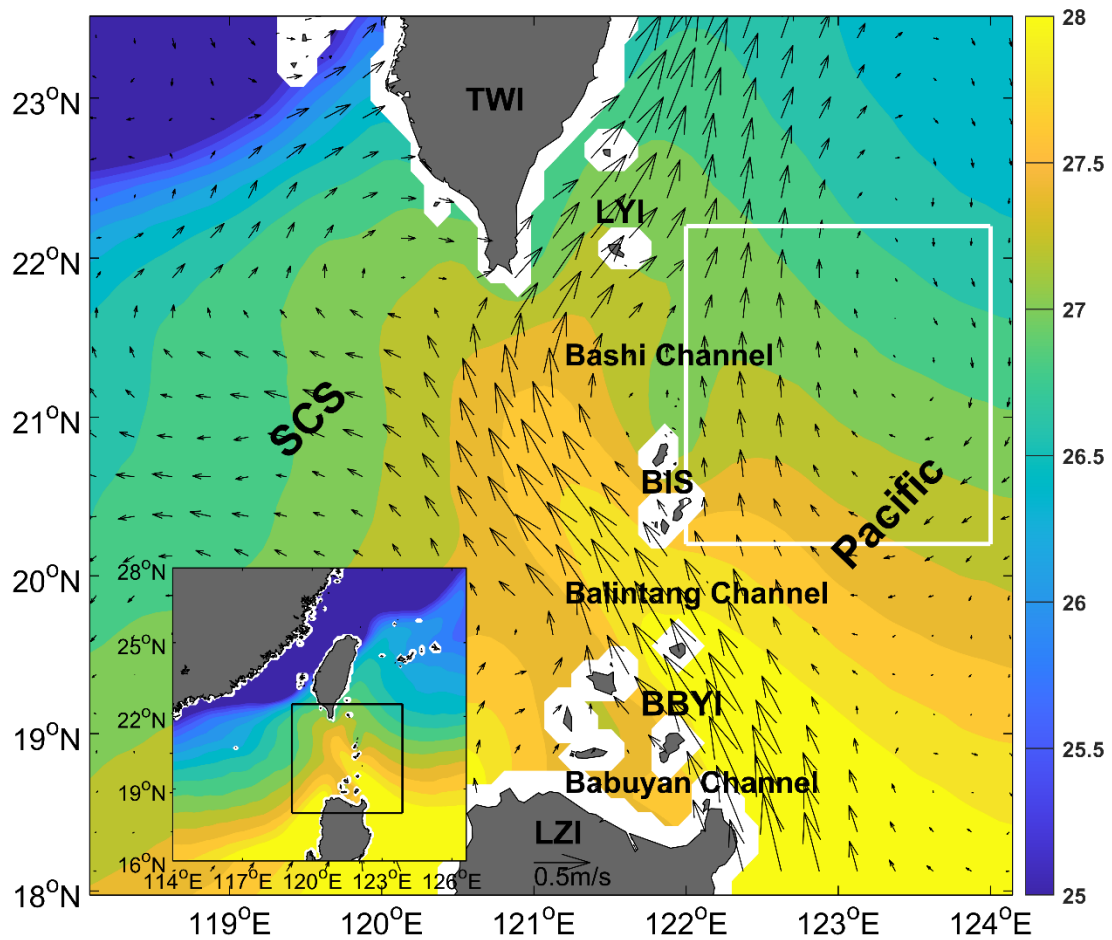
38 Mesoscale eddies interaction is an important focus of previous studies on mesoscale eddies in
39 the LS. Jing and Li (2003) used satellite remote-sensing observation data to discover a cyclonic
40 mesoscale cold eddy around Lanyu Island to the northeast of the LS. They pointed out that the
41 formation of the Lanyu cold eddy was the result of the joint action of the meandering Kuroshio
42 overshooting and conservation of the potential vorticity. Sun *et al.* (2016b) believed that the
43 formation of the Lanyu cold eddy was a process of eddies-eddies interaction. They used satellite
44 observation data and composition analysis to study the Lanyu cold-eddy phenomenon, and pointed

45 out that the combined action of the Kuroshio loop (cyclonic circulation) and an AE from the NWP
46 led to the formation of the Lanyu cold eddy. Based on satellite observation data, *in situ*
47 observation data and numerical modelling data, Zhang *et al.* (2017) studied mesoscale
48 eddies-eddies interaction to the northwest of the LS. They analyzed the energy budget of the
49 Kuroshio invading the SCS, and determined that the northern branch of the anti-cyclonic
50 circulation caused by the Kuroshio loop had a large horizontal shear stress and thus led to the
51 formation of a CE southwest of Taiwan Island through the barotropic instability.

52 Previous studies showed that mesoscale eddies-eddies interaction can cause particle and
53 energy exchange and often occurs in the vicinity of the LS (Sun *et al.*, 2016b; Zhang *et al.*, 2017;
54 Sun *et al.*, 2018). Since the LS is an important gap for particle and energy exchange between the
55 SCS and NWP, a logical question is whether this phenomenon of mesoscale eddies-eddies
56 interaction can occur on the east and west sides of the LS and whether it plays an important role in
57 the particle and energy exchange between the SCS and NWP. To explore this issue, we compare
58 sea-surface height anomaly (SSHA) distributions in the SCS when a CE occurs and when an AE
59 occurs on the east side of the LS (Figure 2). The specific process is described in detail in Section
60 3.1. Figure 2 shows that when an AE (a CE) occurs on the east side of the LS, a CE (an AE) forms
61 on the west side of the LS, which was observed in the *in situ* observation data (Huang *et al.*, 2019).
62 This is referred to in this article as the counter-rotating eddy-pair phenomenon.

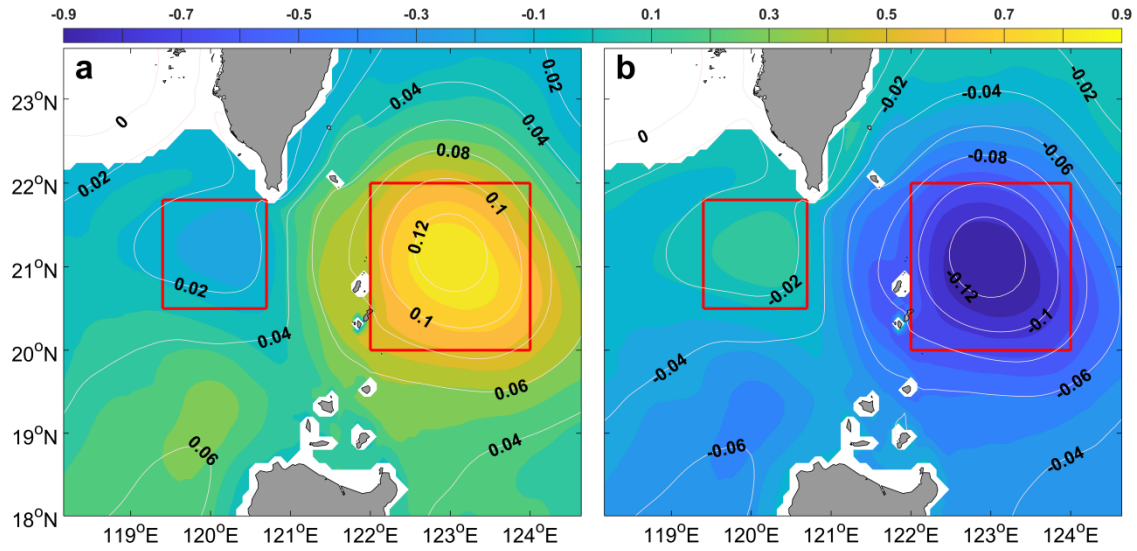
63 To our knowledge, this is the first time a counter-rotating eddy-pair phenomenon in the LS
64 has been proposed, which creates a new form of particle and energy exchange between the SCS
65 and the NWP. The present study will supplement and perfect the theory of particle and energy
66 exchange between the SCS and NWP. We give the statistical characteristics and dynamic

67 mechanism of this phenomenon herein. The rest of this paper is organized as follows. Section 2
 68 briefly introduces the data and methods, Section 3 presents the research results, and Section 4
 69 provides a discussion and conclusion.



70
 71 Figure 1. Climate state of spatial distribution of RSS SST (°C; shading) and CMEMS geostrophic
 72 current (m/s; vectors) from 2003 to 2020. SCS, South China Sea; BIS, Batanes Islands; TWI,
 73 Taiwan Island; LZI, Luzon Island; BBYI, Babuyan Islands; LYI, Lanyu Island. White box borders
 74 20.2–22.2°N, 122–124°E. Extent of the main map is shown as black-bordered box in inset.

75



76

77 Figure 2. Spatial distribution of counter-rotating eddy pair in the LS. Spatial patterns of AE (a) and
 78 CE (b) modes. Panel a (b) corresponds to average state when an AE (a CE) occurred in area
 79 marked by red box on east side of LS from 1993 to 2020. Contours represent SSHA (units of m).
 80 Colors represent sea temperature anomaly (units of °C) at a depth of 300 m. Interval of SSHA is
 81 0.03 m. Red boxes on west and east sides of LS border mark 20.5–21.8°N, 119.4–120.7°E and 20–
 82 22°N, and 122–124°E, respectively. Figure is similar to Figure 3 of Sun *et al.* (2018), and is based
 83 on HYCOM data.

84 2 Data and methods

85 2.1 Data

86 Satellite remote-sensing SSHA, geostrophic current, and geostrophic current anomaly data
 87 were provided by the Copernicus Marine Environment Monitoring Service (CMEMS). The dataset
 88 was generated by the processing system including data from all altimeter missions: Sentinel-3A/B,
 89 Jason-3, HY-2A, Cryosat-2, OSTM/Jason-2, Jason-1, Topex/Poseidon, Envisat, GFO, and
 90 ERS-1/2. The dataset provides global coverage data from January 1, 1993 to August 2, 2021, with
 91 a spatial resolution of 0.25°×0.25° and temporal sampling frequency of 1 d. It also provides one

92 near-real-time component and one delayed-time component. The delayed-time component has
93 been inter-calibrated and provides a homogeneous and highly accurate, long time series of all
94 altimeter data (Pujol and Francoise, 2019), and is chosen for use in this paper.

95 Model data are obtained from the Hybrid Coordinate Ocean Model (HYCOM) model output
96 by the U.S. Naval Research Laboratory. The dataset is based on ocean prediction system output,
97 and the product with the longest time span from 2 October 1992 to 31 December 2012 was chosen
98 from all HYCOM data-assimilation products provided by the HYCOM organization. The dataset
99 is based on ocean prediction system output with a spatial resolution of $0.08^{\circ} \times 0.08^{\circ}$ and 40
100 standard z levels between 80.48°S and 80.48°N . It provides temperature, salinity, sea-surface
101 height, zonal flow, and meridional flow (Wallcraft *et al.*, 2003).

102 The wind dataset was provided by the National Centers for Environmental Information
103 (NCEI). The dataset merges multiple satellite observations with *in situ* instrument and related
104 individual products, provides 6-h, daily, and monthly wind and climate data with a spatial
105 resolution of $0.25^{\circ} \times 0.25^{\circ}$, and contains globally gridded ocean surface vector winds and wind
106 stresses (Zhang *et al.*, 2006).

107 Sea surface temperature (SST) data are from remote-sensing systems (RSSs). The dataset
108 merges the near-coastal capability and high spatial resolution of infrared SST data with
109 through-cloud capabilities of microwave SST data, and has applied atmospheric corrections. It
110 provides daily data with a spatial resolution of $9 \text{ km} \times 9 \text{ km}$ from July 1, 2002 to the present.

111 2.2 Methods

112 2.2.1 Eddy energetic and hydrodynamic instability formula

113 The formation mechanisms of mesoscale eddies in the ocean are commonly attributed to

114 baroclinic and barotropic instabilities (Pedlosky, 1987). The barotropic conversion (BT) and
 115 baroclinic conversion (BC) are manifestations of the baroclinic and barotropic instabilities,
 116 respectively, and they are the major eddy energy sources around the LS (Yang *et al.*, 2013; Zhang
 117 *et al.*, 2013, 2015, 2017). In addition, the wind-stress work (WW) can also contribute to the
 118 formation of eddies (Ivchenko, 1997; Sun *et al.*, 2015). The BT, BC, and WW can be expressed as
 119 follows (Ivchenko, 1997; Oey, 2008):

$$120 \quad BT = - \int \left(\overline{u' \frac{\partial \bar{u}}{\partial x}} + \overline{v' \frac{\partial \bar{v}}{\partial y}} + \overline{u' v' \frac{\partial \bar{u}}{\partial y}} + \overline{u' v' \frac{\partial \bar{v}}{\partial x}} \right) dz, \quad (1)$$

$$121 \quad BC = - \int \frac{g^2}{\rho_0^2 N^2} \left(\overline{u' \rho' \frac{\partial \bar{\rho}}{\partial x}} + \overline{v' \rho' \frac{\partial \bar{\rho}}{\partial y}} \right) dz, \quad (2)$$

$$122 \quad WW = \frac{1}{\rho} \left(\overline{u' \tau'_x} + \overline{v' \tau'_y} \right), \quad (3)$$

123 Where t is time; u, v , and w are the zonal velocity, meridional velocity, and vertical velocity,
 124 respectively, and their positive directions are east, north, and up, respectively. g is the
 125 acceleration due to gravity; N is the buoyancy frequency; ρ is the density of sea water; $\rho_0 =$
 126 $1030 \text{ kg} \cdot \text{m}^{-3}$ is the mean sea-water density; p is the sea pressure; and τ_x and τ_y are the zonal
 127 and meridional components of the wind stress, respectively. x, y , and z are the conventional
 128 east-west, north-south, and up-down Cartesian coordinates, respectively. The depth integrals for
 129 BT and BC are from 400 m to the sea surface. The overbar denotes a time average over 70 d, the
 130 primes denote deviations from the average value of 35 d before and after this day, and the other
 131 symbols and notations are standard. From Figures 6 and 8, it can be seen that the counter-rotating
 132 eddy-pair phenomenon occurs, develops, and disappears from $t = -36$ to $t = 36$, i.e., approximately
 133 70 d. Therefore, the period is chosen to be 70 d. We have made several attempts to set the period
 134 between 65 and 80 d, and they will not affect our basic conclusion. BT and BC were calculated
 135 from HYCOM data. CMEMS surface-current velocity data and NCDC wind data were used to

136 calculate WW.

137 2.2.2 Vorticity budget equation

138 To examine the influence of the vorticity change, we applied the vorticity budget equation

139 (Muller,1995; Kuo and Tseng, 2021):

$$140 \quad \frac{\partial \zeta}{\partial t} = -u \frac{\partial \zeta}{\partial x} - v \frac{\partial \zeta}{\partial y} - (\zeta + f) \nabla \cdot \vec{u} - v \frac{\partial f}{\partial y} + \frac{1}{\rho^2} \left(\frac{\partial \rho}{\partial x} \frac{\partial P}{\partial y} - \frac{\partial \rho}{\partial y} \frac{\partial P}{\partial x} \right) - v \frac{\partial^2 \zeta}{\partial^2 z}, \quad (4)$$

141 Where $\zeta = \frac{\partial v}{\partial x} - \frac{\partial u}{\partial y}$ is the relative vorticity, t is time, f is the Coriolis parameter, P is the

142 sea-water pressure, and $\nu = 1.004 \times 10^{-6}$ is the kinematic viscosity coefficient.

143 x, y, z, u, v , and ρ in formula (4) are as defined in formulas (1)-(3). The items on the right-hand

144 side of the equation are, from left to right, the zonal advection, meridional advection, stretching,

145 beta, baroclinic, and diffusion terms.

146 2.2.3 Definition of modes and intensity index of counter-rotating eddy-pair phenomenon

147 When an AE (a CE) in the NWP gradually approaches the northern LS, a CE (an AE)

148 gradually forms on the west side of the LS, and we define it as an AE (a CE) mode of the

149 counter-rotating eddy-pair phenomenon, as shown in Figures 2a, 3a, and 6 (Figures 2b, 3b, and 8).

150 To reflect the intensity of counter-rotating eddy-pair phenomenon, we must construct an

151 intensity index. As this phenomenon mainly involves the difference of SSHA between the east and

152 west sides of the LS, the index is defined as the time series of the SSHA in the east red box of

153 Figure 2 (expressed as $SSHA_{east}$) minus that in the west red box of Figure 2 (expressed as $SSHA_{west}$),

154 which is shown in Figure 3a and can be expressed as $Index = SSHA_{east} - SSHA_{west}$.

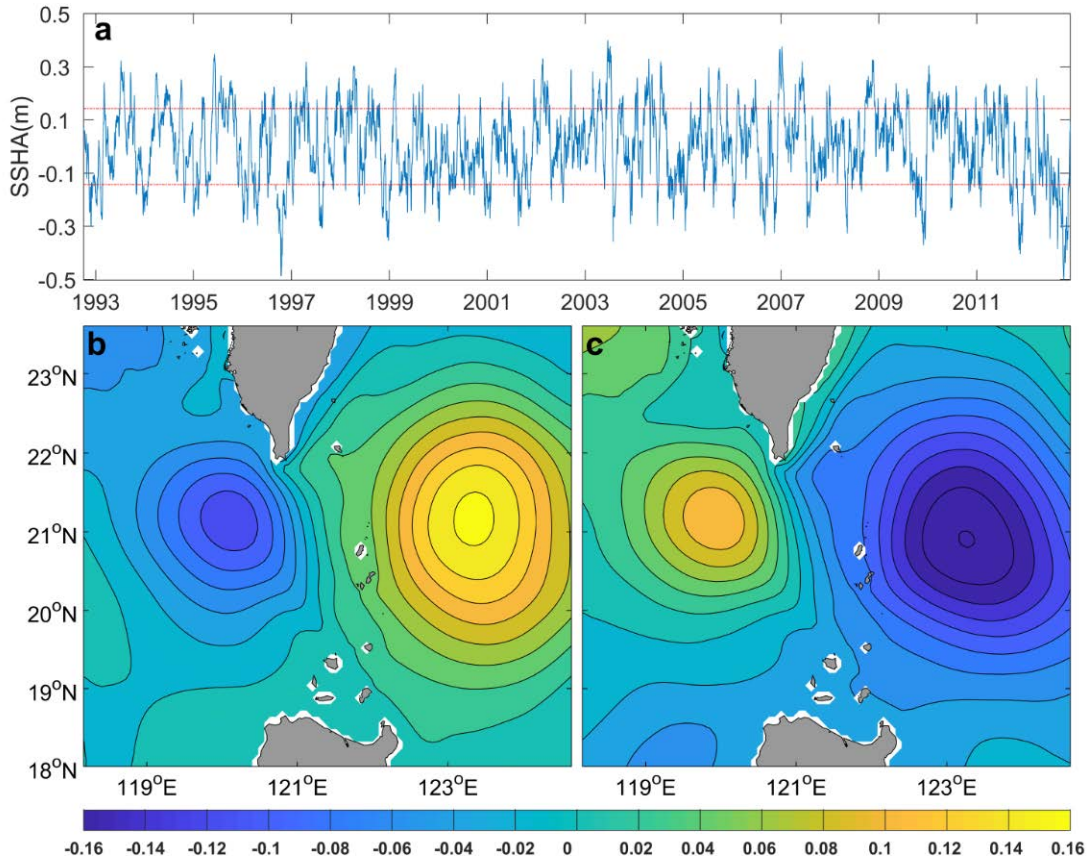
155 3 Results

156 3.1 Identification of counter-rotating eddy pair in LS

157 Based on cluster analysis, which is the same as the clustering method used by Sun *et al.*

158 (2018), the SSHA and sea-temperature anomaly (STA) are determined based on the days when an
159 AE and a CE exist on the east side of the LS (shown in the white box in Figure 1), respectively.
160 Figure 2a shows that the SSHA in the red box on the east side of the LS increases from the outside
161 to inside, which means that there is an AE. Owing to geostrophic balance and mass conservation,
162 the AE causes convergence of sea water, leading to down-welling in its center, subsequently
163 leading to an increase in the temperature in the deep ocean. This is verified by the fact that the
164 STA in the red box on the east side of the LS gradually increases from outside to inside and the
165 value is highest in the center. In addition, the SSHA in the red box on the west side of the LS
166 decreases from outside to inside and the STA is negative, indicating the presence of a weak CE.
167 According to the definition of modes of the counter-rotating eddy pair given in Section 2.2.3, the
168 SSHA pattern in Figure 2a can be identified as an AE mode of the counter-rotating eddy pair.

169 Figure 2b is similar to Figure 2a, but for a CE and an AE on the east and west sides of the LS,
170 respectively, its SSHA pattern can be identified as an AE mode of the counter-rotating eddy pair.
171 According to the intensity index defined in Section 2.2.3, the SSHA is constructed based on the
172 days when the positive and negative intensity index values are more than one standard deviation
173 from the mean, as shown in Figures 3b and 3c. Figure 3b (3c) shows that an AE (a CE) on the east
174 side of the LS corresponds well to a CE (an AE) on the west side of the LS, and can well reflect
175 the AE (CE) mode of a counter-rotating eddy pair in the LS. It also shows that we can well
176 identify this phenomenon according to the intensity index, and, furthermore, that the positive and
177 negative intensity indexes correspond to AE and CE modes, respectively, of this phenomenon.



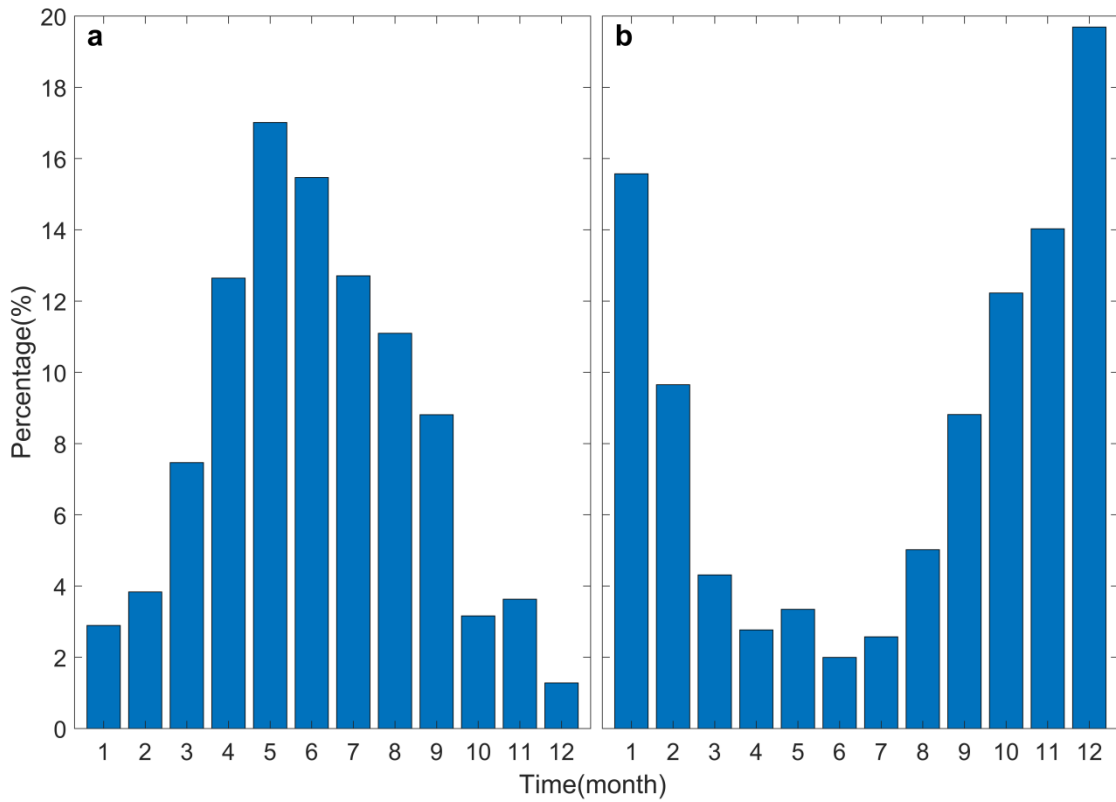
178

179 Figure 3. Time series of intensity index of counter-rotating eddy pair in LS (a). Red dotted line
 180 above (below) represents the sum (difference) of one time the standard deviation and the average
 181 value of the time series. Composition of SSHA for positive (b) and negative (c) intensity-index
 182 days. SSHA interval is 0.02 m. Figure based on HYCOM data.

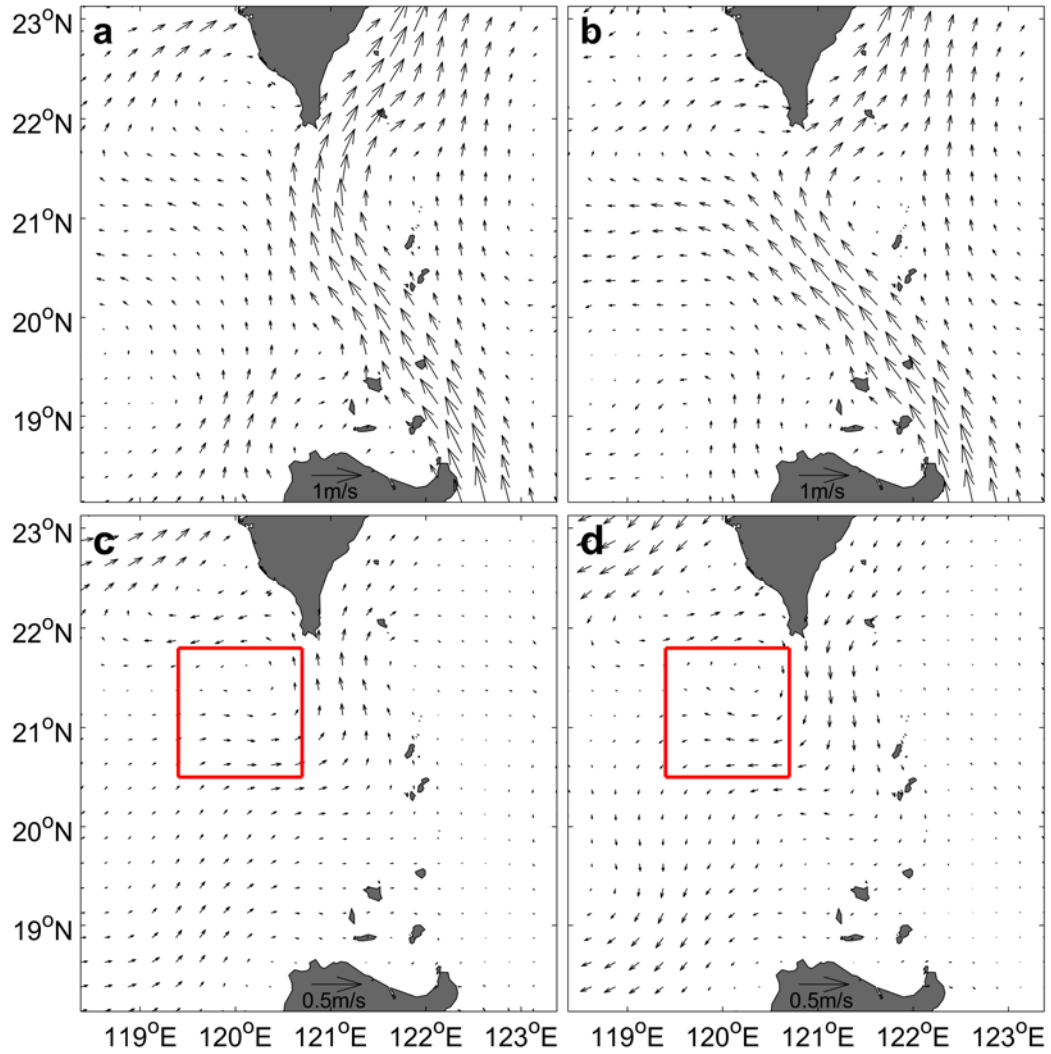
183 3.2 Seasonal variation of counter-rotating eddy pair in LS

184 We counted the temporal distribution of the positive and negative intensity index values in a
 185 statistical sense. Figure 4a (4b) shows that most of the AE (CE) mode of the instances of the
 186 counter-rotating eddy pair occur in the summer (winter) half of the year. The first two months with
 187 the highest incidences of the AE (CE) mode are May and June (December and January), and their
 188 occurrence rates are 17.01% and 15.47% (19.69% and 15.57%), respectively. We constructed the
 189 geostrophic current in May and June (Figure 5a) and in December and January (Figure 5b). The
 190 patterns of the Kuroshio Current in Figures 5a and 5b exhibit as the “Leap” and “Loop” patterns

191 of the Kuroshio in the LS, which illustrates that the Leap and Loop patterns of the Kuroshio
 192 contribute to the occurrence of the AE and CE modes, respectively, of the counter-rotating eddy
 193 pair. Figure 5c (5d) shows that the geostrophic current anomaly in the northern LS is northward
 194 (southward). It produces positive (negative) vorticity through horizontal velocity shear on the west
 195 side of the LS, and then contributes to the formation of a CE (an AE) on the west side of the LS.
 196 We discuss the dynamic mechanism of the counter-rotating eddy-pair phenomenon in detail in
 197 Section 3.3.



198
 199 Figure 4. Seasonal distribution of occurrence rate for positive (a) and negative (b) intensity
 200 indexes.



201

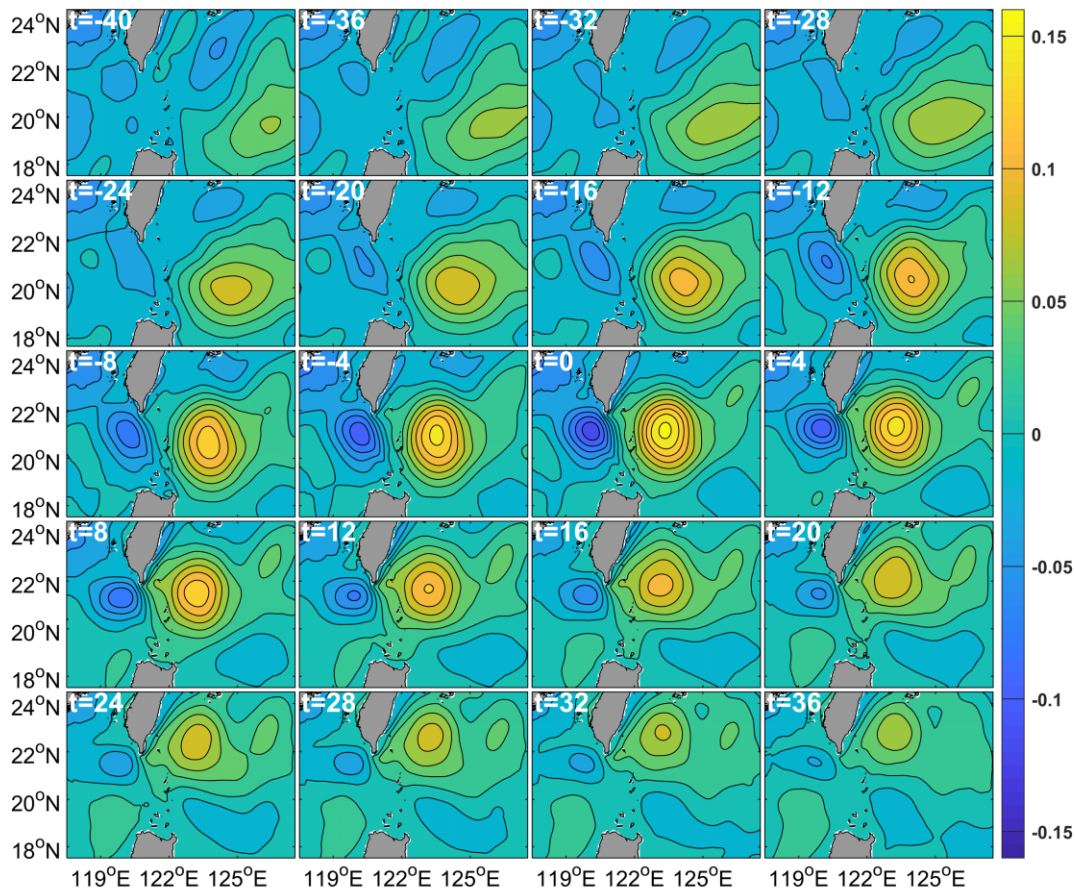
202 Figure 5. Climatic distributions of geostrophic current in May and June (a) and in December and
 203 January (b), and of geostrophic current anomaly in May and June (c) and in December and
 204 January (d). Red boxes in c and d outline 20.5–21.8°N, 119.4–120.7°E, which represent the
 205 position of mesoscale eddies on west side of LS. Figure based on CMEMS data.

206 3.3 Evolution of counter-rotating eddy pair in LS

207 Figure 6 shows the spatial evolution of the AE mode of the counter-rotating eddy pair in the
 208 LS. It shows that at the beginning, for example, at $t = -24$, there is a weak AE far from the east
 209 side of the LS, but no CE on the west side of the LS. From $t = -20$ to $t = 0$, as the AE in the NWP
 210 approaches the northern LS, a CE gradually forms on the west side of the LS. At $t = 0$, the AE

211 mode reaches its maximum. Then, from $t = 4$ to $t = 36$, as the AE in the NWP gradually moves
212 away from the northern LS, the CE on the west side of the LS gradually weakens until it finally
213 dies out.

214 The growth and weakening of a mesoscale eddy must be accompanied by a change in its
215 relative vorticity. Figure 7a shows that as the AE on the east side of the LS approaches and then
216 moves away from the northern LS, its relative vorticity initially decreases and then increases,
217 while the relative vorticity of the corresponding CE on the west side of the LS initially increases
218 and then decreases. The maximum negative (positive) value of the time series of the AE (CE) on
219 the east (west) side of the LS reaches $-4.2 \times 10^{-6} \text{ s}^{-1}$ ($3.6 \times 10^{-6} \text{ s}^{-1}$). These time series have good
220 correspondence and their correlation coefficient is -0.97 at the 95% confidence level. Therefore,
221 the temporal variations in the relative vorticity in Figure 7a verify the evolution of the AE mode of
222 the counter-rotating eddy pair in the LS.



223

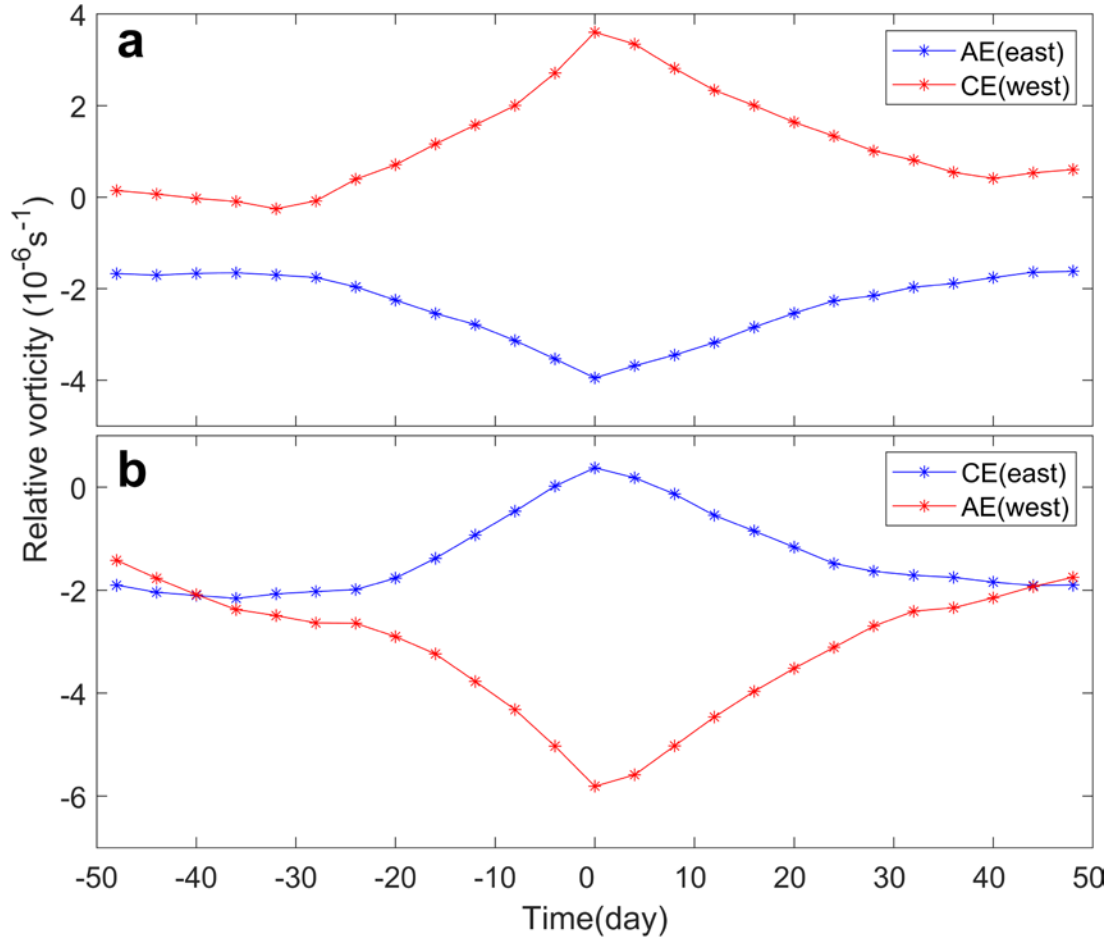
224 Figure 6. Evolution of AE mode of counter-rotating eddy pair in LS based on HYCOM data.

225 Contours and shading both represent SSHA (units of m). SSHA interval is 0.02 m. t value in the

226 top left-hand corner of each panel denotes the days before (negative value) or after (positive value)

227 AE mode of counter-rotating eddy pair reached the maximum (t=0). t = 0 corresponds to the time

228 of Figure 3b.



229

230 Figure 7. Distribution of relative vorticity in area bordered by red boxes in Figure 2. Panel a,
 231 relative vorticity of AE mode over time. Blue (red) line represents time series of relative vorticity
 232 of AE (CE) on east (west) side of LS, which corresponds to Figure 6. Panel b, relative vorticity of
 233 CE mode over time. Blue (red) line represents time series of relative vorticity of CE (AE) on east
 234 (west) side of LS, which corresponds to Figure 8. Figure based on HYCOM data.

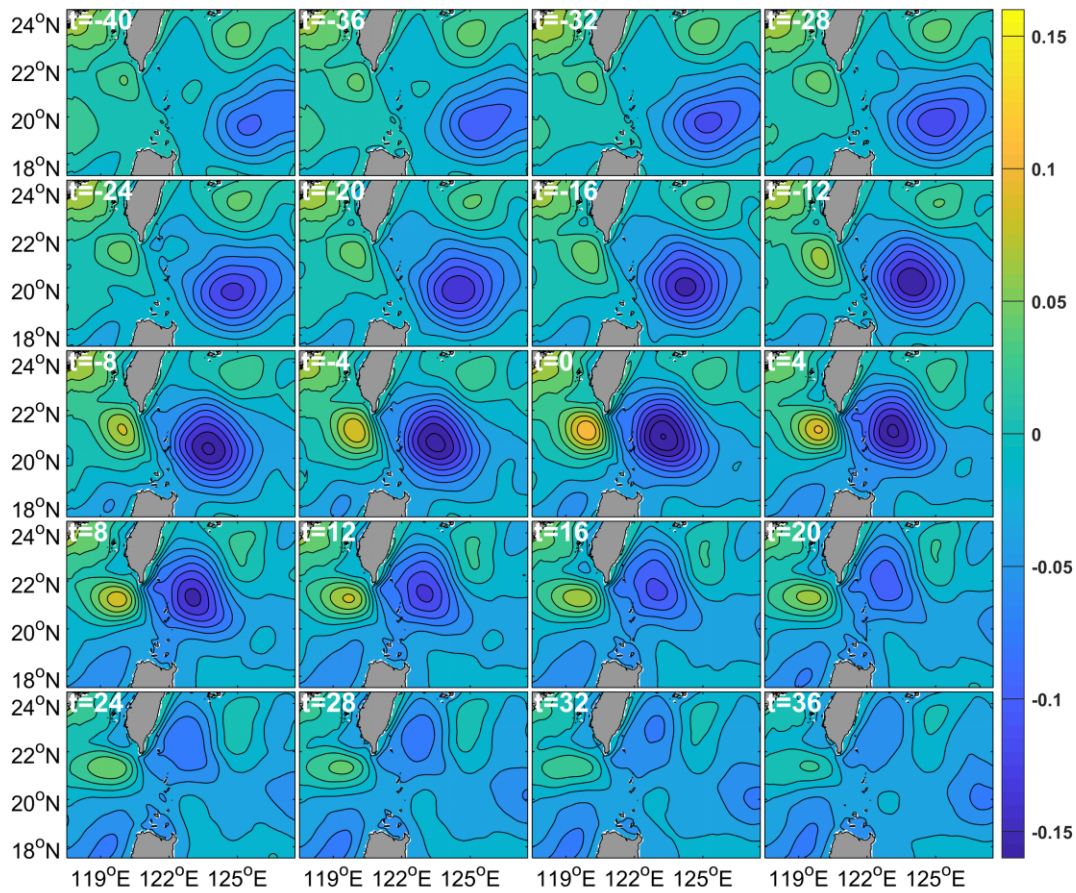
235 Figure 8 plots the CE mode of the counter-rotating eddy pair in the LS. It shows that at the
 236 beginning, for example, at $t = -32$, there is a weak CE far from the east side of the LS, but no AE
 237 on the west side of the LS. From $t = -28$ to $t = 0$, as the CE in NWP approaches the northern LS,
 238 an AE gradually forms on the west side of the LS. At $t = 0$, the CE mode of the evolution of the
 239 counter-rotating eddy pair reaches the maximum. Then, from $t = 4$ to $t = 36$, as the CE in the NWP

240 gradually moves away from the northern LS, the AE in the west side of the LS gradually weakens
241 until it finally dies out. Figure 7b plots the CE mode and shows that as the CE on the east side of
242 the LS approaches and moves away from the northern LS, its relative vorticity initially increases
243 and then decreases, while the relative vorticity of the corresponding AE on the west side of the LS
244 initially decreases and then increases. The maximum positive (negative) value of the time series of
245 the CE (AE) on the east (west) side of the LS can reach $0.48 \times 10^{-6} \text{ s}^{-1}$ ($-6.7 \times 10^{-6} \text{ s}^{-1}$). These time
246 series have good correspondence and their correlation coefficient is -0.96 at the 95% confidence
247 level. Therefore, the temporal variations in the relative vorticity in Figure 7b verify the evolution
248 of the AE mode of the counter-rotating eddy pair in the LS. The evolution of the AE and CE
249 modes of the counter-rotating eddy pair in the LS is also reflected by the satellite observations
250 (Figures 9 and 10).

251

252

253



254

255 Figure 8 Evolution of CE mode of counter-rotating eddy pair in LS based on HYCOM data.

256 Contours and shading both represent SSHA (units of m). SSHA interval is 0.02 m. t in the top

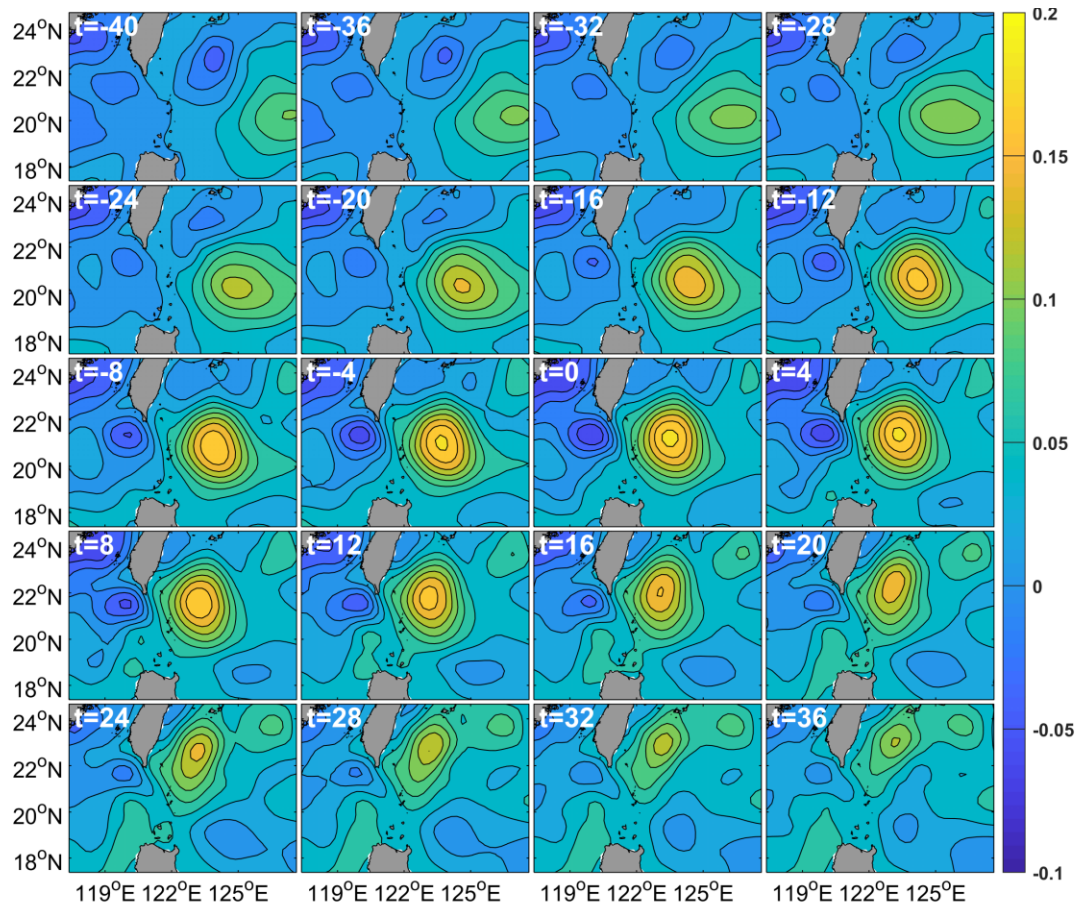
257 left-hand corner of each panel denotes the days before (negative value) or after (positive value) the

258 CE mode of the counter-rotating eddy pair reached the maximum (t=0). t = 0 corresponds to time

259 of Figure 3b.

260

261



262

263 Figure 9 Evolution of AE mode of counter-rotating eddy pair in LS based on CMEMS data.

264 Contours and shading both represent SSHA (units of m). SSHA interval is 0.02 m. t in the top

265 left-hand corner of each panel denotes days before (negative value) or after (positive value) the

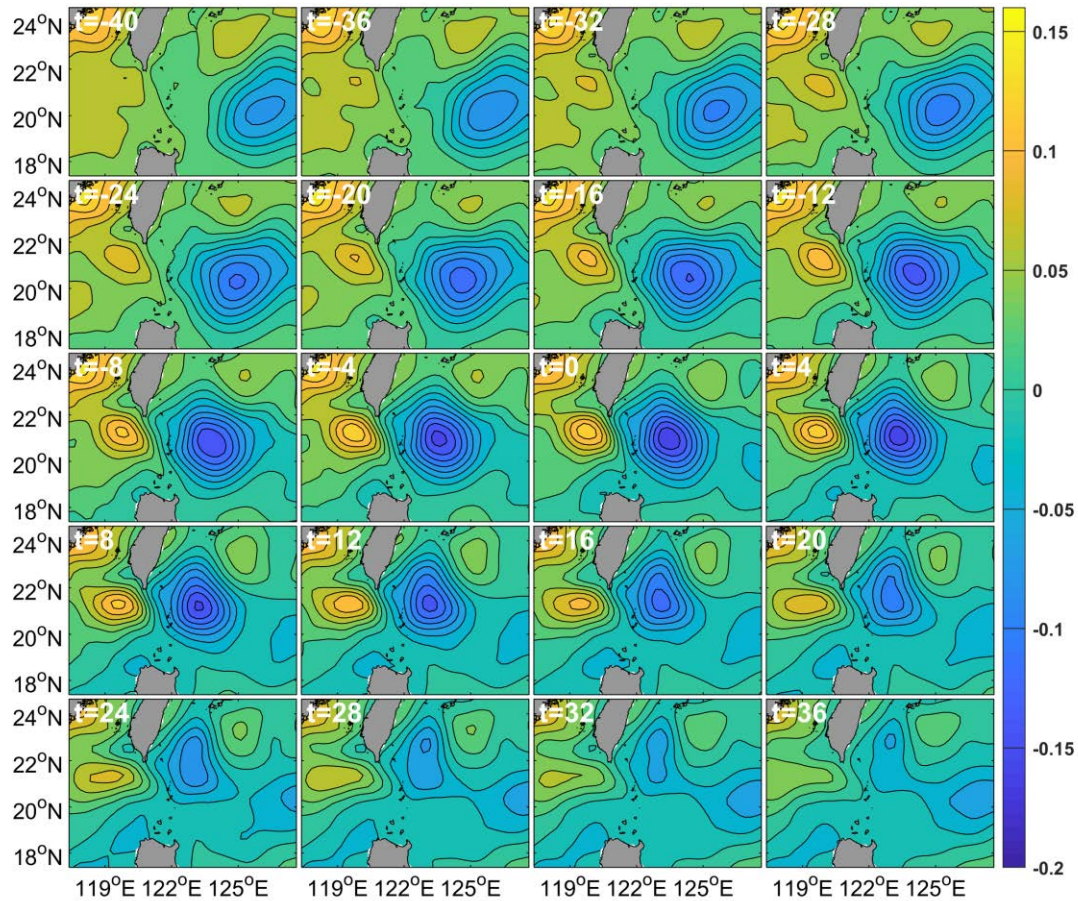
266 AE mode of counter-rotating eddy pair reached the maximum ($t=0$). $t = 0$ corresponds to time of

267 Figure 3b.

268

269

270



271

272 Figure 10 Evolution of CE mode of counter-rotating eddy pair in LS based on CMEMS data.

273 Contours and shading both represent SSHA (units of m). SSHA interval is 0.02 m. t in the top

274 left-hand corner of each panel denotes days before (negative value) or after (positive value) the

275 CE mode of counter-rotating eddy pair reached the maximum ($t=0$). $t = 0$ corresponds to time of

276 Figure 3b.

277 3.4 Formation mechanism of counter-rotating eddy pair in LS

278 Zhang *et al.* (2017) reported that CEs mainly formed due to the barotropic instability caused

279 by horizontal velocity shear of the Kuroshio Loop current southwest of Taiwan Island. Huang *et al.*

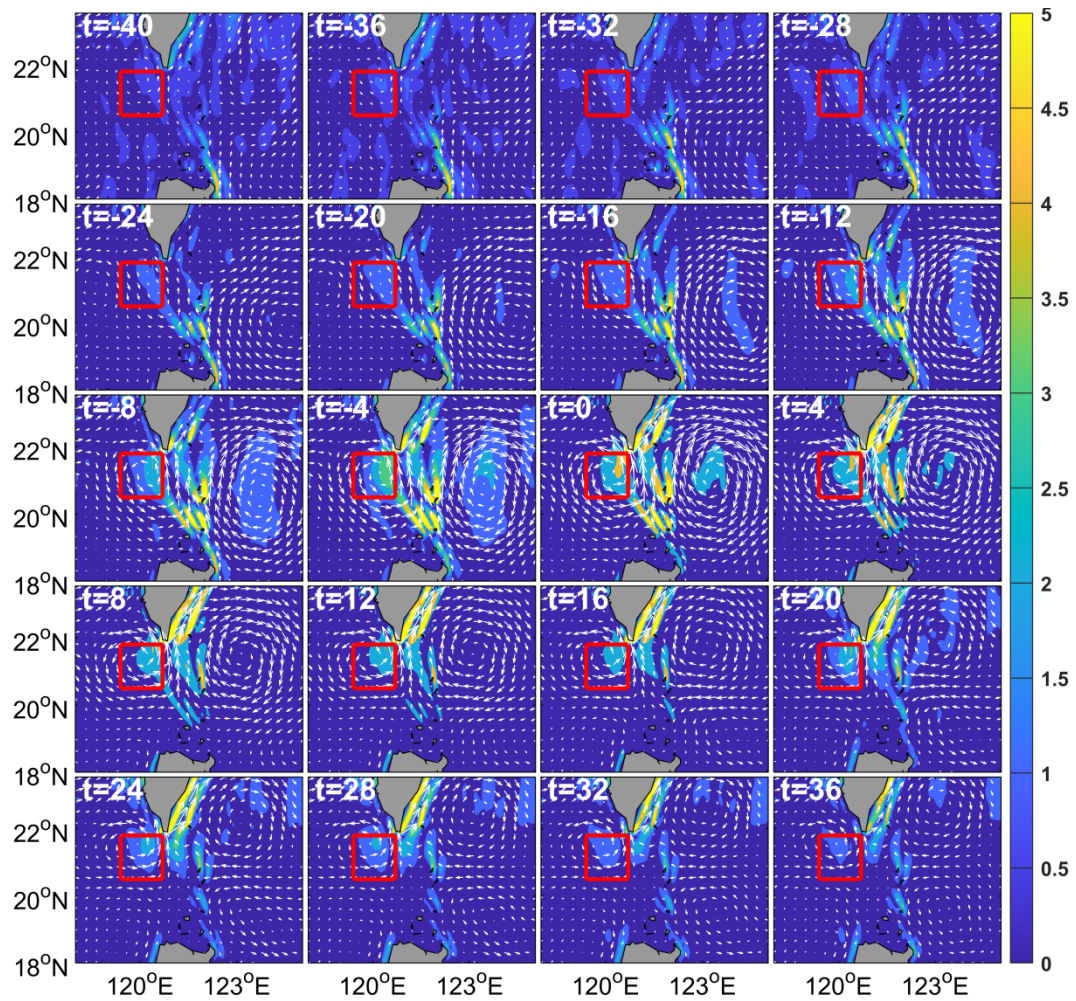
280 (2019) discovered that an AE from the NWP caused a CE to form on the west side of the LS via

281 horizontal velocity shear. In addition, Figures 3b and 3c show that the dense contour of the SSHA

282 means that there are strong current anomalies and thus strong horizontal velocity shear at the

283 junction of the AE and CE. Therefore, we investigated the role of horizontal velocity shear in the
284 formation of a counter-rotating eddy in the LS.

285 Because meridional horizontal velocity shear is weak, we only show the zonal velocity shear.
286 Figure 11 shows that from $t = -40$ to $t = 0$, as the AE on the east side of the NWP gradually
287 approaches the northern LS, the absolute value of the zonal horizontal velocity shear ($\frac{\partial v}{\partial x}$)
288 gradually increases, and a CE gradually forms and strengthens on the west side of the LS. From t
289 $= 0$ to $t = 36$, as the AE gradually moves away from the northern LS, the absolute value of the
290 zonal horizontal velocity shear gradually decreases, and the CE on the west side of the LS
291 gradually weakens. Figure 12 plots the CE mode of the counter-rotating eddy pair in the LS and
292 shows a similar corresponding evolution process. This demonstrates that there is good
293 correspondence between the zonal horizontal velocity shear and evolution process of the
294 counter-rotating eddy pair.



295

296 Figure 11 Evolution process of absolute value of zonal horizontal velocity shear ($\frac{\partial v}{\partial x}$) for AE

297 mode of counter-rotating eddy pair in LS based on HYCOM data. Shading represents zonal

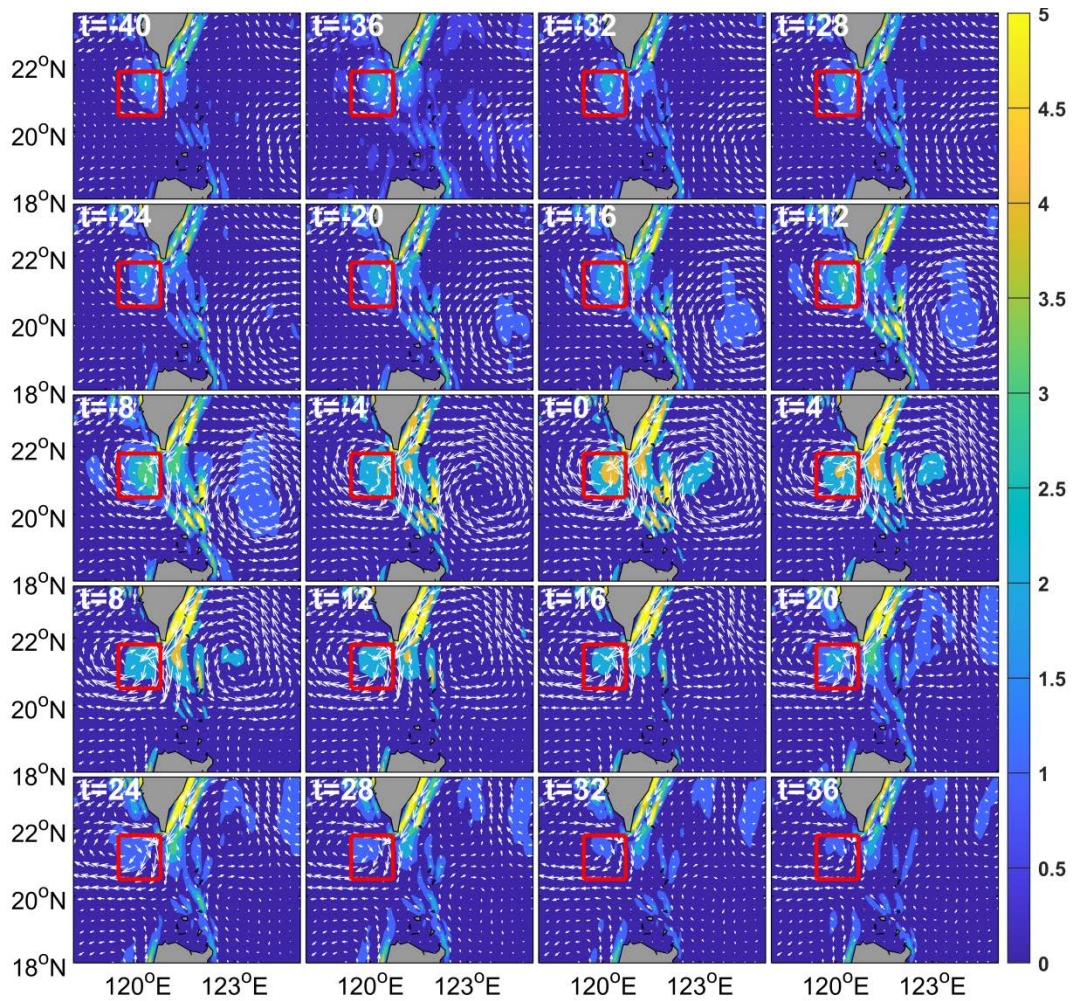
298 horizontal velocity shear (units of 10^{-6} s^{-2}). Vector represents the current anomaly. t in the top

299 left-hand corner of each panel denotes days before (negative value) or after (positive value) the

300 AE mode of counter-rotating eddy pair reached the maximum ($t = 0$). $t = 0$ corresponds to time of

301 Figure 3b. Red boxes on west side of LS cover $20.5\text{--}21.8^\circ\text{N}$, $119.4\text{--}120.7^\circ\text{E}$ and represent

302 location of CE on west side of LS.



303

304 Figure 12 Evolution process of absolute value of zonal horizontal velocity shear ($\frac{\partial v}{\partial x}$) for CE

305 mode of counter-rotating eddy pair in LS based on HYCOM data. Shading represents zonal

306 horizontal velocity shear (units of 10^{-6} s^{-2}). Vector represents current anomaly. t in top left-hand

307 corner of each panel denotes days before (negative value) or after (positive value) the AE mode of

308 counter-rotating eddy pair reached the maximum (t = 0). Time t = 0 corresponds to time of Figure

309 3b. Red boxes on west side of LS cover 20.5-21.8°N, 119.4-120.7°E and represent the location of

310 CE on west side of LS.

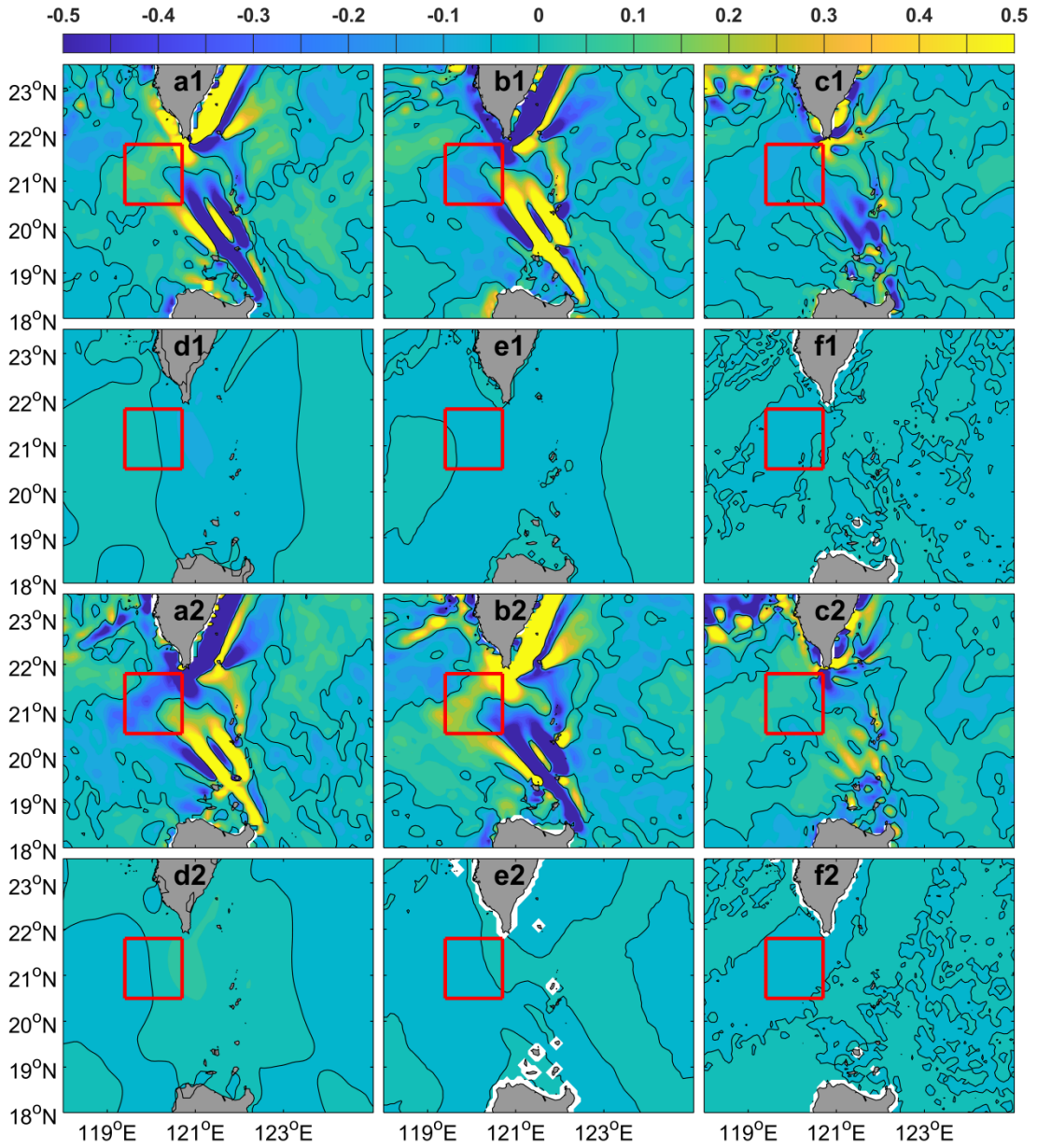
311 However, Figure 11 (12) shows that zonal horizontal velocity shear only occurs on the

312 right-hand side of the red box; that is, on the right-hand side of the CE (AE). How does the

313 horizontal velocity shear pass to the entire CE (AE)? To answer this question, we used the

314 vorticity budget equation. Figures 13a1–f1 plot the AE mode of the counter-rotating eddy pair and
315 show the respective contributions of the zonal advection, meridional advection, stretching, beta,
316 baroclinic, and diffusion terms of the vorticity budget equation. Compared to the stretching, beta,
317 baroclinic, and diffusion terms, the values of the zonal advection and meridional advection terms
318 in the red box are large. However, most of the values of the meridional advection term in the red
319 box are negative. Only positive vorticity advection can lead to formation of a CE, which suggests
320 that the zonal advection term is the main cause of CE formation in the red box. To further test this
321 conclusion, Figure 14a shows the correspondence between the relative vorticity anomaly and
322 zonal advection of the vorticity in the red box in Figure 13, illustrating that there is good
323 correspondence and their correlation coefficient is as high as 0.96 at the 95% confidence level.
324 Therefore, we conclude that the zonal advection term plays the most important role in vorticity
325 transport and contributes to the formation of the CE on the west side of the LS.

326 Figures 13a2–f2 are plots the CE mode of the counter-rotating eddy pair and shows that,
327 compared to the stretching, beta, baroclinic, and diffusion terms, the values of the zonal advection
328 and meridional advection terms in the red box are large. However, most of the values of the
329 meridional advection term in the red box are positive. Only negative vorticity advection can lead
330 to formation of an AE, which implies that the zonal advection term is the main cause of AE
331 formation in the red box. To further test this conclusion, Figure 14b shows the correspondence
332 between the relative vorticity anomaly and zonal advection of vorticity, illustrating that there is
333 good correspondence and their correlation coefficient is as high as 0.84 at the 95% confidence
334 level. Therefore, we conclude that the zonal advection term plays the most important role in
335 vorticity transport and contributes to the formation of the AE on the west side of the LS.



336

337 Figure 13. Vorticity budget equation for (a1–f1) AE mode of counter-rotating eddy pair and

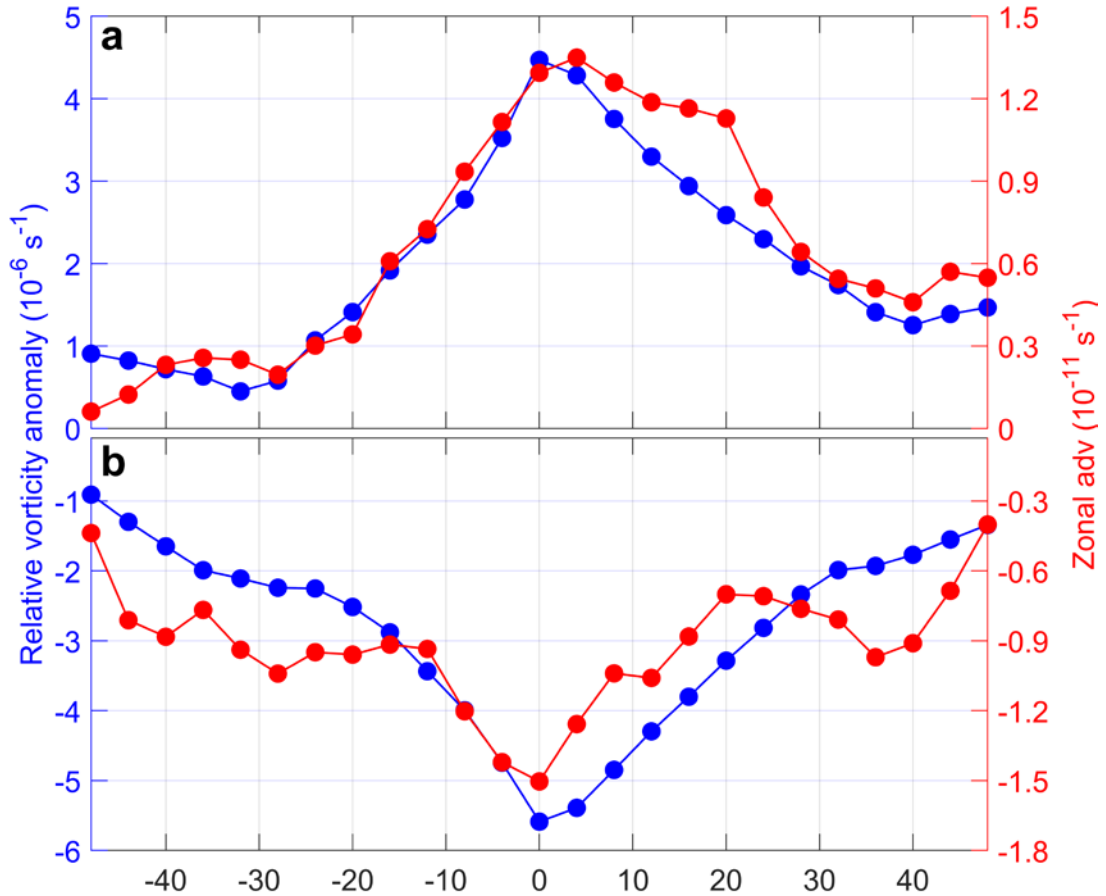
338 (a2–f2) CE mode of counter-rotating eddy pair. a1 and a2 represent the zonal advection term, b1

339 and b2 the meridional advection term, c1 and c2 the stretching term, d1 and d2 the beta term, e1

340 and e2 the baroclinic term, and f1 and f2 the diffusion term. Units are 10^{-10} s^{-2} . Red boxes on west

341 side of LS border cover $20.5\text{--}21.8^\circ\text{N}$, $119.4\text{--}120.7^\circ\text{E}$, and represent location of CE or AE on west

342 side of LS. Black solid line represents the zero contour. Figure based on HYCOM data.

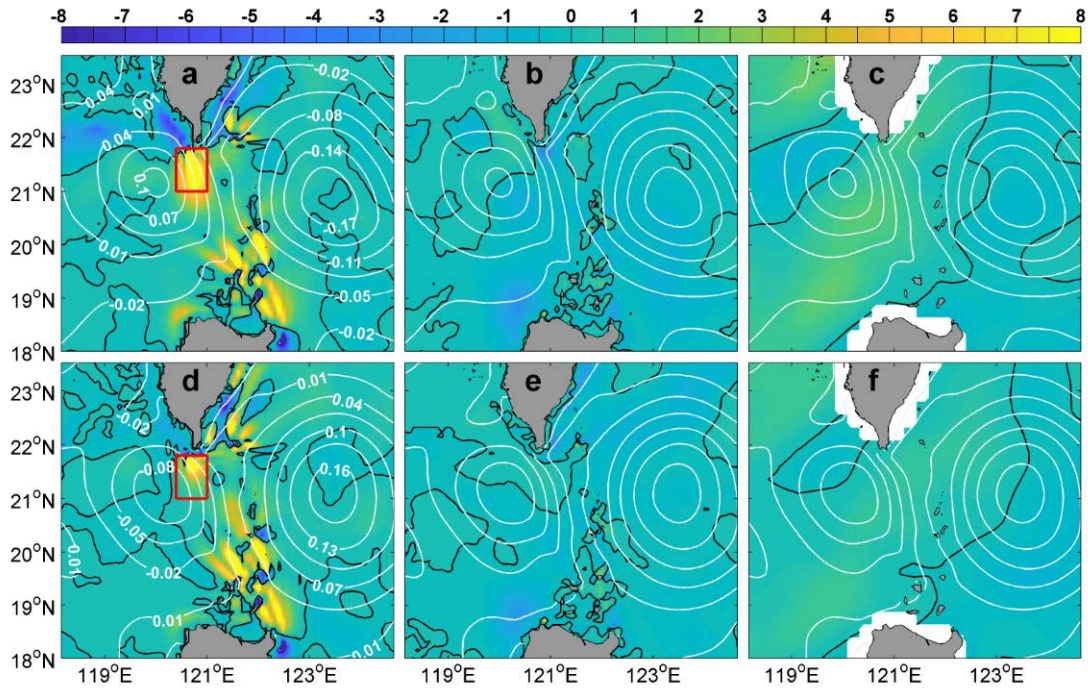


343

344 Figure 14. Distribution of relative vorticity anomaly and zonal advection of vorticity
 345 surrounded by red boxes in Figure 13 for AE (a) and CE (b) modes of counter-rotating eddy pair
 346 in LS.

347 We proposed above that the horizontal velocity shear caused by the mesoscale eddy on the east
 348 side of the LS is transported westward through zonal advection, resulting in the formation of a
 349 counter-rotating mesoscale eddy on the west side of the LS. Horizontal velocity shear will
 350 inevitably lead to barotropic instability. Now, we verify our conclusion from the perspective of
 351 energy. Figures 15a, 15b, and 15c show that, compared to the BC and WW values, the BT values
 352 in the LS are large and most of the values are positive, especially in the area surrounded by the red
 353 box in Figure 15a, which is the junction of the AE and CE. This means that the BT plays the most
 354 important role in formation of the AE on the west side of the LS.

355 Figures 15d, 15e, and 15f show the BT, BC, and WW, respectively, corresponding to the AE
 356 mode of the counter-rotating eddy pair in the LS. The description and dynamic mechanism of the
 357 AE mode are similar to those of the CE mode of the counter-rotating eddy pair in the LS, so the
 358 details will not be discussed here.



359 Figure 15. BT based on HYCOM data ($10^{-5} \text{ m}^3 \text{ s}^{-3}$) represented by colors (a, d); BC based on
 360 HYCOM data ($10^{-5} \text{ m}^3 \text{ s}^{-3}$) represented by colors (b, e); WW based on CMEMS surface velocity
 361 data and NCDC wind data ($10^{-5} \text{ m}^3 \text{ s}^{-3}$) represented by colors (c, f). Red box borders 21°N–
 362 21.8°N, 120.4°E–121°E. White contours represent SSHA contours of. Panels a, b, and c (d, e, and
 363 f) plot CE (AE) mode of counter-rotating eddy pair in LS.

365 4 Discussion and conclusions

366 In this study, based on satellite observation data and HYCOM re-analysis data, the
 367 counter-rotating eddy pair in the LS is investigated. The phenomenon of counter-rotating eddy
 368 pairs is defined as the stage when an AE (a CE) in the NWP gradually approaches the northern LS,
 369 and a CE (an AE) forms on the west side of the LS. This phenomenon exhibits obvious seasonal

370 variation; that is, the AE mode mainly occurs in the summer half of the year, while the CE mode
371 mainly occurs in the winter half of the year. The mean durations of the AE and CE modes are both
372 approximately 70 d. The Leap and Loop patterns of the Kuroshio Current contribute to the
373 occurrence of the AE and CE modes, respectively, of counter-rotating eddy pairs. Based on the
374 vorticity budget equation and energy analysis, the dynamic mechanism of the occurrence of a
375 counter-rotating eddy pair is as follows. The AE (CE) in the NWP causes a positive (negative)
376 vorticity anomaly through horizontal velocity shear on the west side of the LS, and the positive
377 (negative) vorticity anomaly is transported westward by the zonal advection of the vorticity,
378 finally leading to the formation of a CE (an AE) on the west side of the LS. This conclusion is also
379 verified by barotropic instability based on the energy analysis.

380 When we investigated the question of how the horizontal velocity shear passes to the entire
381 CE or AE in Section 3.4, we found that the magnitudes of the meridional and zonal advection
382 terms are roughly the same. Because the meridional advection term has the opposite effect of CE
383 (AE) formation in the west side of the LS for the AE (CE) mode of the counter-rotating eddy pair,
384 we confirmed that the zonal advection term plays a main role in horizontal velocity shear
385 transportation. However, since the magnitude of the meridional advection term is very large, it
386 may play a role in the ocean dynamic process of the LS, which deserves further study.

387 The results presented in this study are preliminary and several problems require further
388 research. The occurrence probability of a counter-rotating eddy pair in the LS must be determined.
389 The counter-rotating eddy pair phenomenon involves spatiotemporal variations in two mesoscale
390 eddies on both sides of the LS, and it is difficult to provide a quantifiable definition of this
391 phenomenon for a single event. For example, how far apart must the mesoscale eddies on the east

392 and west sides of the LS be to define them as a counter-rotating eddy pair. We preliminarily
393 calculated that the incidence of this phenomenon is approximately 5%.

394 Another problem to solve involves threshold of the NWP mesoscale eddies entering the SCS,
395 and what role the Kuroshio Current plays in the counter-rotating eddy-pair phenomenon in the LS.
396 In this study, our illustration of the counter-rotating eddy pair phenomenon does not include the
397 mean current field, which means that the influence of the Kuroshio Current is not considered.
398 However, the role of the Kuroshio in energy transfer is still worthy of further study. Numerical
399 simulations can be useful to address this issue. Our study provides new perspective on particle and
400 energy exchange, and further perfects the theory of particle and energy exchange between the SCS
401 and NWP.

402

403 **Acknowledges**

404 The authors would like to acknowledge several data sets used in this paper. Satellite remote
405 sensing geostrophic current data and sea level anomaly were obtained from the CMEMS, the
406 HYCOM reanalysis data were downloaded from HYCOM organization, the data set of wind was
407 provided by National Climate Data Center. Sea surface temperature data comes from Remote
408 Sensing System. This study was supported by National Natural Science Foundation of China
409 (grant number 41806019), National Key R&D Program of China (2019YFD0901305), Key R&D
410 projection of Zhejiang Province (2020C03012), National Natural Science Foundation of China
411 (No.41776012), State Key Laboratory of Tropical Oceanography (South China Sea Institute of
412 Oceanology Chinese Academy of Sciences) open topics (grant number LTO2011), Key R&D
413 project of Guangdong Province (2020B1111030002), Major science and technology project of

414 Sanya YZBSTC (SKJC-KJ-2019KY03). We thank LetPub (www.letpub.com) for its linguistic
415 assistance during the preparation of this manuscript.

416

417 **Reference**

- 418 Huang Z, Zhuang W, Hu J, et al. Observations of the Luzon Cold Eddy in the northeastern South
419 China Sea in May 2017[J]. *Journal of Oceanography*, 2019, 75(5): 415-422.
- 420 Jing C, Li L. An initial note on quasi-stationary, cold-core Lanyu eddies southeast off Taiwan
421 Island[J]. *Chinese Science Bulletin*. 48(19): 2101-2107.
- 422 Kuo Y, Tseng Y. Influence of anomalous low-level circulation on the Kuroshio in the Luzon Strait
423 during ENSO[J]. *Ocean Modelling*, 2021, 159, 101559.
- 424 Ivchenko V O, Treguier A M, and Best S E. A kinetic energy budget and internal instabilities in the
425 fine resolution antarctic model, *Journal of Physical Oceanography*, 1997, 27:5-22.
- 426 Liu Y, Dong C, Guan Y, et al. Eddy Analysis in the Subtropical Zonal Band of the North Pacific
427 Ocean[J]. *Deep Sea Research Part I*, 2012, 68:54-67.
- 428 Lu J, Liu Q. Gap-leaping Kuroshio and blocking westward-propagating Rossby wave and eddy in
429 the Luzon Strait[J]. *Journal of Geophysical Research Oceans*, 2013, 118(3):1170-1181.
- 430 Muller P. Ertel's potential vorticity theorem in physical oceanography[J]. *Reviews of Geophysics*,
431 1995, 33(1):67-97.
- 432 Oey L Y. Loop Current and Deep Eddies[J]. *Journal of Physical Oceanography*, 2008, 38(7): 1426
433 -1449.
- 434 Pedlosky J. *Geophysical Fluid Dynamics*, 1987, 2nd ed., 710 pp., Springer, N. Y.
- 435 Pujol M, Françoise M. Product user manual for sea level SLA products. Copernicus Monitoring
436 Environment Marine Service (CMEMS), 2022, <https://doi.org/10.48670/moi-00148>.
- 437 Remote Sensing Systems (RSS): <https://www.remss.com/measurements/ sea-surface-temperature/>.

438 Sun R, Ling Z, Chen C, et al. Interannual variability of thermal front west of Luzon Island in
439 boreal winter[J]. *Acta Oceanologica Sinica*, 2015, (34):108.

440 Sun R, Wang G, Chen C. The Kuroshio bifurcation associated with islands at the Luzon Strait[J].
441 *Geophysical Research Letters*, 2016a, 43(11):5768-5774.

442 Sun R, Gu Y, Li P, et al. Statistical characteristics and formation mechanism of the Lanyu cold
443 eddy[J]. *Journal of Oceanography*, 2016b, 72(4):641-649.

444 Sun R, Zhai F, Gu Y. The Four Patterns of the East Branch of the Kuroshio Bifurcation in the
445 Luzon Strait[J]. *Water*, 2018, 10(12).

446 Sun R, Zhai F, Zhang G, et al. Cold Water in the Lee of the Batanes Islands in the Luzon Strait[J].
447 *Journal of Ocean University of China*, 2020, 19(6):10.

448 Wallcraft A, Carroll S N, Kelly K A, et al. Hybrid Coordinate Ocean Model (HYCOM) Version
449 2.1 User's Guide. HYCOM consortium, 2003. [https://www.hycom.org/dataserver/gofs-3pt0](https://www.hycom.org/dataserver/gofs-3pt0/reanalysis)
450 /reanalysis.

451 Yang H, Wu L, Liu H, et al. Eddy energy sources and sinks in the South China Sea[J]. *Journal of*
452 *Geophysical Research Oceans*, 2013, 118(9):4716-4726.

453 Zhang Z, Zhao W, Tian J, et al. A mesoscale eddy pair southwest of Taiwan and its influence on
454 deep circulation[J]. *Journal of Geophysical Research Oceans*, 2013, 118(12):6479-6494.

455 Zhang Z, Zhao W, Tian J, et al. Spatial structure and temporal variability of the zonal flow in the
456 Luzon Strait[J]. *Journal of Geophysical Research Oceans*, 2015, 120(2).

457 Zhang Z, Zhao W, Qiu B, et al. Anticyclonic Eddy Sheddings from Kuroshio Loop and the
458 Accompanying Cyclonic Eddy in the Northeastern South China Sea[J]. *Journal of Physical*
459 *Oceanography*, 2017, 47(6):1243-1259.

460 Zhang H M, Reynolds R W, Bates J J, et al. Blended and gridded high resolution global sea
461 surface wind speed and climatology from multiple satellites: 1987-present. American
462 Meteorological Society 2006 Annual Meeting, Vol. 2. [https://www.ncei.noaa.gov/products](https://www.ncei.noaa.gov/products/blended-sea-winds)
463 /blended-sea-winds
464
465
466
467